

Large Fatty Acid-derived A β 42 oligomers Form Ring-like Assemblies

Wenhui Xi, Dexter N. Dean, Ulrich H.E. Hansmann and Vijayaraghavan Rangachari*

*** corresponding author**

ABSTRACT

As the primary toxic species in the etiology of Alzheimer disease (AD) are low molecular weight oligomers of A β , it is crucial to understand the structure of A β oligomers for gaining molecular insights into AD pathology. We have earlier demonstrated that in the presence of fatty acids A β 42 peptides assemble as 12-24mer oligomers. These Large Fatty Acid-derived Oligomers (LFAOs) exist predominantly as 12mers at low, and 24mers at high concentrations. The 12mers are more neurotoxic than the 24mers and undergo self-replication, while the latter propagate to morphologically distinct fibrils with succinct pathological consequences. In order to glean into their functional differences and similarities, we have determined their structures in greater detail by combining molecular dynamic simulations with biophysical measurements. We conclude that the LFAO 12mers form a double-layered hexamer ring (6 x 2) structure in which A β units are present in an S-shaped conformation while the structure of 24mers is a double-layered dodecamer ring (12 x 2). A closer inspection of the (6 x 2) and (12 x 2) structures reveal that a concentration and pH dependent molecular reorganization is involved in the assembly of 12 to 24mers, which seems to be the underlying mechanism for the observed biophysical and cellular properties of LFAOs.

INTRODUCTION

One of the hallmarks of Alzheimer disease (AD) pathology is the deposition of amyloid- β (A β) peptide fibrillar aggregates as plaques in brains of patients. The neuronal loss, however, seems to be triggered primarily by low-molecular weight (LMW) oligomers that are formed earlier than the high-molecular weight fibrils during the aggregation process (1). Therefore, there is a growing interest in isolating LMW oligomers and deriving their atomistic structure and dynamics. However, the transient nature and heterogeneity of the oligomers makes their isolation and characterization, either from endogenous or exogenous sources, difficult. As a consequence, deriving structural models, as needed for understanding their toxicity mechanism and mode of propagation, poses a challenge.

The Rangachari Lab has developed a method for generating A β 42 12-24mer assemblies in the presence of saturated fatty acids A β 42 12-24mer assemblies, called large fatty acid-derived oligomers (LFAOs) (2-7). At higher concentrations, LFAOs convert from the 12mer species to more disperse distribution of 12- 24mer oligomers (2). This concentration-dependent transition is significant because the 12mers self-replicate in the presence of monomers, and are more apoptotic than the 24mers (2). On the other hand, the 24mers faithfully propagate towards morphologically-unique fibrils and induce acute cerebral amyloid angiopathy (CAA) in transgenic mice (3). Therefore, it is imperative to obtain atomistic insights into the differences between the 12mer and 24mer LFAOs, as well as the transition from one form to the other, in order to better understand their unique properties. Unfortunately, due to some of the aforementioned reasons, the structures of these LFAOs have so far not been resolved.

Guided by computational investigations of the Hansmann laboratory, we present in this paper structural models for 12mer and 24mer LFAOs, and a mechanism for the transition from

one to the other assembly. Derivation of these models relies on the advanced computational techniques developed in the Hansmann lab. These have been already used in previous work to study the various polymorphs seen in amyloids (8-11), and to probe the factors that modulate conformational switching in amyloids (11). Combining these advanced computational methodologies with novel biophysical experiments, we conclude that the 12mers prefer to form two-layered rings, each a hexamer (6 x 2), while 24mers transition to another species of two-layered assemblies, here each ring a dodecamer (12 x 2). We also eliminate the possibility of a single dodecamer ring (12 x 1) structure for 12mers, and of four stacked hexamer rings (6 x 4) as the structure for 24mers. The two newly introduced models allow to explain the experimentally observed conformational-dynamics of LFAOs, to identify the key residues involved in conformational switching, and hint at the structural basis for the different pathogeny of LFAO 12mers and 24mers.

MATERIALS

Lyophilized stocks of synthetic A β 1-42 WT peptide were procured from the Yale School of Medicine peptide synthesis facility (New Haven, CT). C12:0 NEFA was purchased from NuCheck Prep, Inc. (Elysian, MN), while ANS was purchased from Sigma-Aldrich Corp. (St. Louis, MO). All other buffers, reagents, and consumables were procured from Thermo Fisher Scientific, Inc. (Waltham, MA).

METHODS

Molecular dynamics simulation. The oligomers models presented in this article are based on previous work where we constructed a series of N-fold ring-like A β 42 oligomer models

(8), including six-fold and twelve-fold models of A β (11-42) that are characterized by S-shaped chain configurations forming three β -strands linked by two turn regions. The chains in a ring are kept together by hydrophobic contacts in the region of residues 20-28 and an inter-chain salt bridge K16-D23. These models are the starting point in our construction of the (6 x 2), (6 x 4) and (12 x 2) models described later.

Our simulations rely on the software package GROMACS 5.1.5 (12) and employ the AMBER ff99SB-ildn (13) force field for proteins and TIP3P water (14) as solvent, a choice also employed by us in our previous work (15). The temperature of 300K and a pressure of 1 bar are controlled by v-rescale thermostat (16) and Parrinello-Rahman barostat (17). The bond-lengths are restrained by the LINCE algorithm (18) and SETTLE algorithm (19) allowing us to use a time step of 2 fs for integration. Protein and solvent are put into a box with side length and periodic boundary conditions of 13.28 nm (for 6 x 2), 18.86 nm (for 12 x 2), and 13.31 nm (for 6 x 4), and electrostatic interactions are calculated by the particle mesh Ewald (PME) method (20). All trajectories are followed for 20ns, with only the last 10 ns used for analysis.

Most of our analysis are carried out within the tool set provided by GROMACS, with snapshots of configurations visualized by VMD (21). The distance between residues are defined as the average distance between heavy atoms in the sidechains of each residue; for example, the NZ atom on K16 and the OD1 atom on D23 are used to calculate the inter-chain salt-bridge between residues K16 and D23. We measure the solvent accessible surface area (SASA) by both the *g_sasa* and *POPS* (22) software tools, the later allowing one to separate the hydrophobic and hydrophilic areas. Since the two methods use different definitions of surface area, values may differ slightly. The binding energy are approximated with *MMPBSA.py* in AmberTools(23), with the setting *igb=8* for the GBSA part.

A β monomer and oligomer purification. A β monomers and oligomers were purified as described previously (4). Briefly, 0.5-1 mg of synthetic peptide was weighed into a sterile microcentrifuge tube and resuspended in 500 μ L of 10 mM NaOH. After incubation at 25 °C for 30 min, the sample was loaded onto a Superdex-75 HR 10/30 size exclusion column pre-equilibrated in 20 mM Tris, pH 8.0 using either an AKTA FPLC (GE Healthcare) or BioLogic DuoFlow (BioRad) purification system. Fractions of 500 μ L were collected at a constant flow rate of 0.5 mL/min. A β concentrations were determined using intrinsic tyrosine absorbance ($\epsilon = 1450 \text{ cm}^{-1} \text{ M}^{-1}$ at 276 nm) on a Cary 50 UV-Vis spectrometer (Agilent Technologies). To generate LFAOs, A β monomers (50-60 μ M) were incubated with 5 mM C12:0 NEFA and 50 mM NaCl at 37 °C for 48 hours. LFAOs were then centrifuged at 20,000 g for 20 min before being purified via SEC as described above.

ANS binding assay. ANS binding experiments were done as described previously (2). For experiments at varying pH, LFAOs were exchanged into 20 mM Tris at the appropriate pH using a 3.5 kDa molecular weight cut-off Slide-A-Lyzer MINI Dialysis Device (Thermo Fisher Scientific) following the manufactures protocol. Upon the addition of 100 μ M ANS followed by 1 min of equilibration, fluorescence measurements of LFAOs (8, 6, 4, 2, 1, or 0.5 μ M) were collected on a Cary Eclipse instrument (Agilent Technologies) by scanning the emission spectrum between 400 and 650 nm upon excitation at 388 nm. The area under the curve for each respective pH or NaCl titration experiment were then normalized from 0-1, and plotted as shown in the text. The data presented are representative of three independent experiments.

Circular dichroism spectroscopy. Data were collected on a Jasco J-815 spectropolarimeter attached with a Peltier temperature controller. To a solution of LFAOs (1 or 8 μ M), sodium dodecyl sulfate (SDS) was added to a final concentration of 1% (wt/v), followed by

heating from 10-90 °C (ramp rate = 0.5 °C/min) while monitoring the signal at 206 nm every 1 min (hold time = 30 s, DIT = 32 s, bandwidth = 5 nm). The data was processed by normalizing from 0-1 (as shown in Fig 4a), followed by determining the apparent standard free energy using the Gibbs-Helmholtz equation (as shown in Fig 4b). The data presented are representative of three independent experiments.

RESULTS

LFAOs are two-layered rings. Detailed biophysical characteristics of LFAOs were obtained previously (2-5, 7). LFAOs display the presence of two aggregate distributions corresponding to sedimentation coefficients 5S and 7S (Fig 1a, reproduced from (6)), corresponding to 12mers and more heavy assemblies of 12-24mers. The secondary structure determined by far-UV circular dichroism (CD) shows β -sheet structure that remains unchanged in an order of magnitude concentration difference (Fig 1b; reproduced from (2)). However, two oligomer distributions were observed within the same concentration range on immunoblots (Fig 1b; *inset*); a band corresponding to 50-60 kDa (12mer) at 0.5 μ M, and an additional band at 80-110 kDa (24mer) at 8 μ M (2). This concentration-dependent transition can be monitored by the increase in solvent exposed hydrophobic surfaces, as determined by 1-anilino naphthalene sulfonate (ANS) binding (Fig. 1c, ●), and is consistent with an apparent dissociation constant (K_d) of 0.1 μ M (2). This transition between 12mer and 24mer LFAOs is absent in both monomer (□) and fibril (△) control samples (Fig. 1c, reproduced from (2)).

In a recent paper (24), we have shown that unlike the more common, but less toxic A β 40, A β 42 polypeptide can form naturally pore-like trimers and larger oligomers. This is because A β 42 chains are able to assume a S-shaped three-stranded motif, while A β 40 peptides

are not stable in this form and instead take U-shaped conformations in fibrils (15). The models presented in our previous work (24) were the starting point for our investigation, and guided by the experimental size measurements we conjecture that the 12mer is organized as two hexameric units stacked on top of one another (6 x 2) (Fig 2a) (8). In such an arrangement, the hydrated diameter of the oligomer measures 14-15 nm with a height of 3-4 nm, giving a flattened disc-like appearance. Note that oligomers with a similar structure have also been reported already earlier for A β peptide-fragments of various length (25-27). The solvated diameter of the (6 x 2) structure is in close agreement with the size estimates from dynamic light scattering (DLS), and sedimentation velocity analyses, which indicate an hydrodynamic diameter that ranges between 10-13 nm (Fig 2b), and a bimodal sedimentation coefficient between 4S and 7S (Fig 1a), respectively (6). Atomic force microscopy (AFM) analyses indicate spherical punctuate dot-like morphology for LFAOs (Fig 2c). A comparison of the dimensions derived from the AFM data and those from (6 x 2) model shows a good agreement between the two (Fig 2d). We premise that a large tip radius of AFM cantilever (2 nm) is not suitable to detect the cavity within the ring assembly. For the same reason, the shape of height plot was corrected to calculate the actual diameter of the oligomer as indicated in Fig 2c. It is noteworthy that the slight elevation in AFM heights (5-7 nm) than the height of the two layers in 6 x 2 model (3-4 nm) can be accounted for when the oligomer is layered in $\sim 30^\circ$ angle on the mica surface (Fig 2c). On the other hand, the height measurements exclude the possibility of a single-layered dodecamer ring. This observation parallels similar ones observed previously for A β 42 oligomers (27). Note that our structural models are for residues 11-42 in the A β 42 chains as residues 1-10 are flexible in all resolved fibril structures. To evaluate the effect of first 10 residues, we also constructed the full-length A β 42 oligomers for (6 x 2) and (12 x 2) models with the N-terminal segment in the

beginning in a random coil configuration that is allowed to relax in a molecular dynamics simulation over 10 ns. The orientation of the first ten residues stayed random, and their sole effect was that the diameter of (6 x 2) oligomers changed from 10.5 to 14.6 nm.

In order to model the heavier LFAO 24mers, two possible models were considered: a tetramer of hexamers (6 x 4), or a dimer of dodecamers (12 x 2). Both models are largely in agreement with previous experimental results in their dimensions and size seen by AFM, which range between 14-20 nm of height observed (2, 3, 6) (Fig 2e and 2f). In order to distinguish between the two possible models, we performed detailed atomistic molecular dynamics (MD) simulation for all three A β 11-42 oligomer models, the (6 x 2) 12mer and the two 24mer models (6 x 4) and (12 x 2). These simulations allow us to evaluate energetics and stability of these models and the transition mechanism between the lighter and heavier species. Note that the experimental measurements were obtained at a pH=8 which was modeled in our simulation by changing the H13 and H14 residues into the deprotonated state (named as HIE state) expected in this neutral/slightly alkaline experimental condition. Each system is studied in two independent runs. In Table 1 we list the solvent accessible surface area (SASA) and the binding energy as approximated by the MMGBSA approach.

Comparing the solvent accessible surface area (SASA) of the three models we note that it's values for (12 x 2) model of the 24mers is about double that of the (6 x 2) 12mer, while the corresponding SASA of the (6 x 4) 24mer model is less than 1.5 times that of the 12mer. This observation supports the experimental data that solvent accessible hydrophobic surface area doubles from LFAO 12mers to 24mers (Fig 1b). Hence, based on the ANS binding data, one can conclude that the (12 x 2) model is a more likely structure adopted by the 24mers. This model

has a diameter of 15.7 nm, which extends to 19.5 nm for the full-sized model (including the first ten N-terminal residues), also in agreement with the experimentally measured dimensions.

This (12 x 2) model for the 24mer is also favored by the binding energies shown also in Table 1. The (12 x 2) structure has binding energies similar (or slightly more favorable) than two times the (6 x 2) model (see the difference $\Delta(A) = E_{(12 \times 2)} - 2 \times E_{(6 \times 2)}$ in Table 1), while the binding energy of the 6 x 4 model is substantially higher than the double of the 6 x 2 model (see the difference $\Delta(B) = E_{(6 \times 4)} - 2 \times E_{(6 \times 2)}$ in Table 1), making this assembly unfavorable. A simple way to understand why the 12 x 2 model is more favorable than the (6 x 4) model is to neglect entropic contributions and to approximate the binding energy of a 12mer by;

$$E_{(6 \times 2)} = (2 \times 6) \times A + 6 \times B + (2 \times 6) \times C,$$

where A is interaction between chains *within* a ring, B the interaction between chains of *neighboring* rings, and C the interaction of chains with *surrounding water* (i.e. proportional to exposed surface). With the same definitions, one finds that the binding energy of a (12 x 2) would be;

$$E_{(12 \times 2)} = (2 \times 12) \times A + 12 \times B + (2 \times 12) \times C,$$

i.e, $\Delta(A) = E_{(12 \times 2)} - 2 \times E_{(6 \times 2)} = 0$. On the other hand, the binding energy of (6 x 4) would be ;

$$E_{(6 \times 4)} = (4 \times 6) \times A + (3 \times 6) \times B + (2 \times 6) \times C,$$

i.e, $\Delta(B) = E_{(6 \times 4)} - 2 \times E_{(6 \times 2)} = 6 \times B - (2 \times 6) \times C$. This difference describes in first approximation how much more unfavorable the (6 x 4) model is over the (12 x 2) model, and results from repulsive interactions between the (6 x 2) 12mers. The histidine side chains at positions 13 and 14 orient themselves towards one side of the hexamer ring in the upper layer, while similar histidines on the congruent A β 42 unit on the lower layer hexamer ring do so on the opposite

side. Hence, the positioning of the histidine chains hinders further association of hexamer rings (leading to steric clashes), which would make a (6 x 4) structure thermodynamically expensive. The above results suggest that the transition between 12mers and 24mers is not a simple stacking of two 12mers, but a reorganization of chains needed because there is a repulsive interaction between (6 x 2) 12mer that prohibits stacking and leads to the large unfavorable binding energy. Instead, a (12 x 2) structure is formed where the histidines (H13 and H14) are moved $\sim 95^\circ$ perpendicular to the axis of the oligomer, thus preventing potential charge repulsion due to protonation. Furthermore, this transition also results in the exposure of hydrophobic residues along either side of oligomer face, see Table 1, evident from increase in ANS binding (Fig 1c).

This scenario is consistent with the observation that the transition between 12mer and 24mer depends on concentration, see (Fig 1b and 1c) (2), and can be understood from the energetics of our (6 x 2) 12mer and (12 x 2) 24mer models. At low concentrations, the 12mers are separated and experience little repulsive forces. At the same time, the gain in energy from forming a 24mer is negligible, and therefore the equilibrium between the two forms shift towards the 12mer. On the other hand, above a critical threshold, the distance between (6 x 2) 12mer rings becomes so close that the repulsive interaction between them becomes noticeable. At that point it becomes energetically more favorable to rearrange and form (12 x 2) assemblies, i.e., the equilibrium is shifted toward the 24mers.

Dynamics based on stability. While the above reasoning is plausible, more evidence is needed to support our models for 12mer and 24mer, and for the implied mechanism for the concentration-dependent transition between the two forms. Since the transition from 12 to 24mer involved exposure of charged histidines (Fig 1b), we reasoned that the transition could involve electrostatic interactions. In an effort to obtain molecular details on such a possibility, we

investigated the effect of buffer pH and salinity on 12 to 24mer transition using the ANS binding assay. This transition was previously established at pH 8.0 in low ionic strength conditions (absence of salt) (■; Fig 3a and 3b). Upon decreasing the pH from 8.0 to 5.0, the 12 to 24mer transition was less pronounced with a decrease in binding affinity (Fig 3a). Similarly, systematically increasing the ionic strength also resulted in a diminished ability of 12mers to convert to 24mers (Fig 3b). The decrease in pH near the isoelectric point (pI) of A β (5.5) resulted in a reduction in propensity of 12- to 24mer conversion. This indicates the direct involvement of favorable electrostatic interactions, as the abrogation of charges (near the pI) diminishes the 12 to 24mer conversion (Fig 3a). Specifically, this indicates the potential involvement of protonation/deprotonation events in such a transition. To further investigate differences in 12mers and 24mers, thermodynamic stability analysis was performed in the presence of a denaturant (sodium dodecyl sulfate, SDS). In these experiments, the conversion of β -sheet structure adopted by LFAOs to an α -helix in the presence of SDS was monitored by far-UV CD at 206 nm as a function of temperature (Fig 4a). The equilibrium data were processed (as described in the experimental) to obtain the apparent Gibbs free energy at 37 °C, which were found to be -0.879 and -0.489 kcal/mol for LFAO 12mer (1 μ M) and 24mer (8 μ M), respectively (Fig 4b). This difference of 0.4 kcal/mol is minimal and insignificant, revealing that both isoforms have similar thermodynamic stability.

In our simulations, we model the switch from neutral conditions to acidic by repeating our simulations of the three systems (the (6 x 2) for the 12mers, and the (6 x 4) and (12 x 2) model for the 24mers), and with protonated histidine 13 and 14, i.e., setting the charge state to positive (called HIP in this paper). All other parameters in the two sets of simulations are identical. Our data for the pH<7 simulations are summarized in Table 2. Comparing binding energies between

charged ($\text{pH} < 7$) and neutral forms, it appears that the energy differences between 24mer (12×2) and 12mer (6×2) form the 24mers in the charged state more favorably than in the neutral state ($(\Delta\Delta G) = \sim 13 \text{ kcal/mol}$). This is unexpected as the experimental data shows a faster transition toward 24 mer at $\text{pH} \geq 7$. Hence, the sharper transition between 12mer and 24mer is *not* because at $\text{pH} \geq 7$ the 24mer is energetically more favored over the 12mer than in acidic conditions. Instead, the sharper transition at $\text{pH} \geq 7$ is because the repulsion between 6×2 is about 70 kcal/mol higher for the +1 charged form than the neutral form (Table 1 and 2). In other words, the repulsion between the 12 mers is larger at low pH values than in the neutral range where a faster 12 to 24mer transition was observed. Hence, at low pH larger concentrations are needed to overcome the stronger repulsion between the 12mer than at neutral or higher pH, leading to a less pronounced transition. Note also that while the SASA does not differ between the charged and neutral forms in (6×2) model, a difference is observed for the (12×2) structure. For neutral (HIE), the (12×2) structure exposes roughly two times (347 \AA^2 ; Table 1) the hydrophobic surfaces as the (6×2) , 12mer (164 \AA^2 ; Table 1), an observation that the experimental results concur with (Fig 1b). This also means they expose similar surface as 2 (6×2), but for HIP, the (12×2) structure exposes more surfaces than 2 (6×2) model, making formation of 24mer less favorable (Table 1 and 2), which further supports the experimental observation.

DISCUSSION

What is the cause for the above described differences between the 12mer and 24mer at low pH and neutral pH that in turn modulate the concentration-dependent transition between 12mer and 24mer? These differences have to be connected with differences in the two

geometries, and with the way these differences change with pH. One possibility is the way residues are exposed to the solvent. Fig. 5 shows the per-residue differences in solvent exposed surface area between HIE and HIP states for (6 x 2) and (12 x 2) structures. While on average the SASA does not differ between charged and neutral forms in (6 x 2) mer, the turn region, t1 between $\beta 1$ and $\beta 2$ (see Fig 2a) is more exposed in HIE than in HIP while most other residues are more exposed in HIP than HIE. A similar picture is seen in the (12 x 2) 24mer, only that here the relative exposure of residues in the turn region in HIE is much smaller, and overall the solvent exposed surface is larger in HIP than in HIE. Hence, our solvent accessible surface differences indicate that the pH-modulation of the transition between 12mer and 24mer involves this turn region.

This observation is confirmed by Fig 6 where the per-residue contributions to the binding energy are shown. The contribution of binding energy for each residue was calculated in three different ways: first, the difference between HIE and HIP states for (6 x 2) and (12 x 2) models (Fig 6a), second, the difference in binding energies between two times that of (6 x 2) model and a (12 x 2) model (Fig 6b). In both cases no clear signal is seen in the figures. However, when looking into the difference in binding energy of two isolated (6 x 2) models minus the binding energy of the (6 x 4) model (Fig 6c), which is a measure for the maximal repulsion between two (6 x 2) models, a clear signal is seen. The only segment where there is a difference between HIE and HIP are residues 20 to 28, which include the turn region between $\beta 1$ and $\beta 2$, and other residues located on packing surface that directly interact with residues on the neighboring fold. For this segment, the binding energy contribution is for neutral pH is similar between two isolated (6 x 2) rings and when fully associated as a (6 x 4) assembly, while under acidic conditions the binding energy contribution from these segment favor isolated (6 x 2) assemblies.

This is consistent with Fig 5a which shows that under acidic conditions the residues in this segment are less exposed to solvent than under neutral conditions.

Visual inspection of this segment in the (6 x 2) model for both HIE and HIP systems shows that this region is slightly more distorted in HIP than in HIE (Fig 7). This distortion is related with (and can be quantified by) a weakening of the salt-bridge between K16 and E22 or D23 (mainly the K16-D23, see (28)) that is formed between neighboring chains. To show this, the average distance of all corresponding salt-bridge pairs between the O¹/O² atoms on D23 and N^ε atom on K16 were calculated, and the distributions of such distances for the HIP and HIE models are shown in Fig 8.

Compared with the neutral state (HIE), the acid state decreases the stability of the inter-chain salt-bridge in the (6 x 2) model. How does the different charge states of the histidine lead to this effect? In HIP, residues 13 and 16 are both positively charged and the repulsive interaction between them could distort the geometry of the salt-bridge between residue K16 and either D23 or E22. In order to quantify the repulsive interaction between the two positively charged H13 and K16, we have calculated the average distance between the mass center of imidazole on H13 and N^ε atoms on K16 on the same chain, and drawn the distribution of distances between H13 and K16 in Fig 8. The geometry in the 24mer (a two-layer dodecamer ring) is such that the different charge states of H13 does not change the average distance between H13 and K16, and therefore also does not weaken the salt bridge K16-D23 (E22), see Fig. 7. On the other hand, for the 12mer (a two-layer hexamer ring) the distribution of distances between residues H13 and K16 is shifted towards larger values for acidic conditions reflecting the repulsive interaction between the two residues under these conditions. This is not seen for the 24mer because for a (12 x 2) structure, the same histidines (H13 and H14) are moved ~ 95

perpendicular to the axis of oligomer, and thus preventing potential charge repulsion due to protonation. The net-effect of this repulsive interaction between the charged histidine and the lysine K16 is a weakening of the salt bridge K16-D23 (E22), (Fig. 8), which in turn reduces the stability of the turn region between the $\beta 1$ and $\beta 2$ strands and the hydrophobic core region for the peptides in the 12mer under acidic conditions. The binding energies (Fig. 6c) indicate that this distortion leads to a larger repulsive interaction between (6 x 2) structure, shifting the equilibrium toward the 12mer.

CONCLUSIONS

Combining a variety of biophysical measurements and molecular dynamics simulations we put forward models for the fatty acid catalyzed A β 42 assemblies called LFAOs. These 12mers and 24mers are ring-like two-layered objects (two hexamer rings in the case of the 12mer, and two dodecamer rings in the case of the 24mer) that appear as punctuate spherical dots in AFM images. Such disc-like oligomers of A β have also been observed by many groups (25-27). Based on AFM imaging, ring-like, spherical low molecular oligomers are observed to be transiently formed before the formation of high molecular weight oligomers, which then laterally associate to form protofibrils (25). Economou and colleagues observed that even at low concentrations, A β 42 but not A β 40, form ring-like hexamers that convert to dodecamers, which consequently seed protofibril formation (26). Our observations on LFAO structure and propagation supporting previous reports add much needed detail. The studies undertaken in our labs have confirmed that LFAOs are ring-like dodecamers at low concentrations (6, 8). Detailed investigations on the mechanism of LFAO propagation suggested that LFAO 24mers are formed at higher concentrations, which grow larger to form a key intermediate on route to fibril

formation in a three-step mechanism (4). Overall, these observations are in agreement to those described previously (25, 27).

Perhaps the intriguing and enigmatic properties of LFAOs are; (i) the ability of 12mers to self-replicate in the presence of monomers, (ii) to convert to 24mers in a concentration dependent manner and, (iii) the striking differences in the pathogenicity of 12 and 24mers. While both oligomeric forms are pathogenic, LFAO 12mers are more apoptotic to neuroblastoma cells than the 24mers (2). LFAOs also induce acute CAA in transgenic mice brains selectively, although it remains unclear which form of LFAO is responsible for this phenotype (3). The results presented here bring out the molecular signatures that are responsible for the structural and functional differences between LFAO 12 and 24mers, and provide insights into the structure and mechanism by which LFAOs behave and become neurotoxic. At elevated concentrations, (6 x 2) LFAOs form 24mers by adopting a (12 x 2) structure accompanied by reorganization in the assembly, which exposes the hydrophobic residues along either side of oligomer face, an observation also supported by an increase in ANS binding. Such a reorganization increases the susceptibility of 24mers for further oligomer associations mediated largely by hydrophobic interactions. This is indeed supported by the fact that LFAO 24mers are able to propagate morphologically distinct fibrils made by repeats of LFAO units (4).

Insights into the molecular underpinnings of oligomer behavior is much needed to understand AD pathology and for future therapeutic interventions. This work is a step toward advancing our knowledge into this critical area, providing insights into the structure and mechanism by which LFAOs behave and become neurotoxic.

AUTHOR CONTRIBUTIONS

VR and UHEH conceptualized and conducted the research. DND performed biophysical experiments and data analysis while WX conducted molecular dynamics simulations and analyzed the results. All authors were involved in manuscript writing and editing.

ACKNOWLEDGEMENTS

The authors would like to thank the following agencies for financial support: National Institute of General Medical Sciences (R01GM120634, to UH and VR), and NSF Graduate Research Fellowship Program (NSF 1445151) (to DND). Simulations were done on the SCHOONER cluster of the University of Oklahoma. The authors declare no conflicts of interest. The authors also thank Ms. Jhinuk Saha for her help with DLS experiments.

REFERENCES

1. Haass, C., and D. J. Selkoe. 2007. Soluble protein oligomers in neurodegeneration: lessons from the Alzheimer's amyloid β -peptide. *Nat. Rev. Mol. Cell Biol.* 8(Copyright (C) 2014 American Chemical Society (ACS). All Rights Reserved.):101-112. 10.1038/nrm2101.
2. Dean, D. N., K. M. Pate, M. A. Moss, and V. Rangachari. 2016. Conformational Dynamics of Specific A β Oligomers Govern Their Ability to Replicate and Induce Neuronal Apoptosis. *Biochemistry* 55(15):2238-2250.
3. Dean, D. N., P. K. Das, P. Rana, F. Burg, Y. Levites, S. E. Morgan, P. Ghosh, and V. Rangachari. 2017. Strain-specific Fibril Propagation by an A β Dodecamer. *Scientific Reports* 7:40787.
4. Dean, D. N., P. Rana, R. P. Campbell, P. Ghosh, and V. Rangachari. 2018. Propagation of an Ab42 Dodecamer Strain Involves a Three-Step Mechanism and a Key Intermediate. *Biophysical Journal* 114(3):539-549.
5. Kumar, A., R. L. Bullard, P. Patel, L. C. Paslay, D. Singh, E. A. Bienkiewicz, S. E. Morgan, and V. Rangachari. 2011. Non-Esterified Fatty Acids Generate Distinct Low-Molecular Weight Amyloid- β (A β 42) Oligomers along Pathway Different from Fibril Formation. *PLoS ONE* 6(4):e18759.
6. Kumar, A., L. C. Paslay, D. Lyons, S. E. Morgan, J. J. Correia, and V. Rangachari. 2012. Specific Soluble Oligomers of Amyloid- β Peptide Undergo Replication and Form Non-fibrillar Aggregates in Interfacial Environments. *J. Biol. Chem.* 287(Copyright (C) 2014 American Chemical Society (ACS). All Rights Reserved.):21253-21264. 10.1074/jbc.M112.355156.

7. Kumar, A., K. M. Pate, M. A. Moss, D. N. Dean, and V. Rangachari. 2014. Self-propagative replication of Abeta oligomers suggests potential transmissibility in Alzheimer disease. *PLoS One* 9(11):e111492.
8. Xi, W., and U. H. E. Hansmann. 2017. Ring-like N-fold Models of Abeta42 fibrils. *7(1):6588*.
9. Zhang, H., W. Xi, and U. H. E. Hansmann. 2017. Fibril-Barrel Transitions in Cylindrin Amyloids. *13(8):3936-3944*.
10. Xi, W., E. K. Vanderford, and U. H. E. Hansmann. 2018. Out-of-Register Abeta42 Assemblies as Models for Neurotoxic Oligomers and Fibrils. *14(2):1099-1110*.
11. Xi, W., and U. H. E. Hansmann. 2018. Conversion between parallel and antiparallel beta-sheets in wild-type and Iowa mutant Abeta40 fibrils. *148(4):045103*.
12. Abraham, M. J., T. Murtola, R. Schulz, S. Páll, J. C. Smith, B. Hess, and E. Lindahl. 2015. GROMACS: High performance molecular simulations through multi-level parallelism from laptops to supercomputers. *SoftwareX* 1-2:19-25.
13. Lindorff-Larsen, K., S. Piana, K. Palmo, P. Maragakis, J. L. Klepeis, R. O. Dror, and D. E. Shaw. 2010. Improved side-chain torsion potentials for the Amber ff99SB protein force field. *Proteins* 78(8):1950-1958.
14. Jorgensen, W. L., J. Chandrasekhar, J. D. Madura, R. W. Impey, and M. L. Klein. 1983. Comparison of simple potential functions for simulating liquid water. *Journal of chemical physics* 79(2):926-935.
15. Xi, W., W. Wang, G. Abbott, and U. H. Hansmann. 2016. Stability of a Recently Found Triple-beta-Stranded Abeta1-42 Fibril Motif. *The journal of physical chemistry. B* 120(20):4548-4557.

16. Bussi, G., D. Donadio, and M. Parrinello. 2007. Canonical sampling through velocity rescaling. *The Journal of chemical physics* 126(1):014101.
17. Berendsen, H. J. C., J. P. M. Postma, W. F. van Gunsteren, and J. Hermans. 1981. Interaction Models for Water in Relation to Protein Hydration. In *The Jerusalem Symposia on Quantum Chemistry and Biochemistry. Intermolecular Forces*. B. Pullman, editor. Springer Netherlands, pp. 331-342.
18. Hess, B., H. Bekker, H. J. C. Berendsen, and J. Fraaije. 1997. LINCS: A linear constraint solver for molecular simulations. *J. Comput. Chem.* 18(12):1463-1472. Article.
19. Miyamoto, S., and P. A. Kollman. 1992. Settle: An analytical version of the SHAKE and RATTLE algorithm for rigid water models. *J. Comput. Chem.* 13(8):952-962. Article.
20. Darden, T., D. York, and L. Pedersen. 1993. Particle mesh Ewald: An N·log(N) method for Ewald sums in large systems. *Journal of chemical physics* 98(12):10089-10092.
21. Humphrey, W., A. Dalke, and K. Schulten. 1996. VMD: visual molecular dynamics. *Journal of molecular graphics* 14(1):33-38, 27-38.
22. Cavallo, L., J. Kleinjung, and F. Fraternali. 2003. POPS: A fast algorithm for solvent accessible surface areas at atomic and residue level. *Nucleic acids research* 31(13):3364-3366.
23. Miller, B. R., T. D. McGee, J. M. Swails, N. Homeyer, H. Gohlke, and A. E. Roitberg. 2012. MMPBSA.py: An Efficient Program for End-State Free Energy Calculations. *Journal of Chemical Theory and Computation* 8(9):3314-3321.
24. Xi, W., and U. H. E. Hansmann. 2017. Ring-like N-fold Models of A β 42 fibrils. *Scientific Reports* 7(1):6588.

25. Fu, Z., D. Aucoin, J. Davis, W. E. Van Nostrand, and S. O. Smith. 2015. Mechanism of Nucleated Conformational Conversion of Abeta42. *Biochemistry* 54(27):4197-4207.
26. Economou, N. J., M. J. Giammona, T. D. Do, X. Zheng, D. B. Teplow, S. K. Buratto, and M. T. Bowers. 2016. Amyloid beta-Protein Assembly and Alzheimer's Disease: Dodecamers of Abeta42, but Not of Abeta40, Seed Fibril Formation. *Journal of the American Chemical Society* 138(6):1772-1775.
27. Galzitskaya, O. V., and O. M. Selivanova. 2017. Rosetta Stone for Amyloid Fibrils: The Key Role of Ring-Like Oligomers in Amyloidogenesis. *Journal of Alzheimer's disease : JAD* 59(3):785-795.
28. Berhanu, W. M., E. J. Alred, and U. H. Hansmann. 2015. Stability of Osaka Mutant and Wild-Type Fibril Models. *The journal of physical chemistry. B* 119(41):13063-13070.

FIGURES

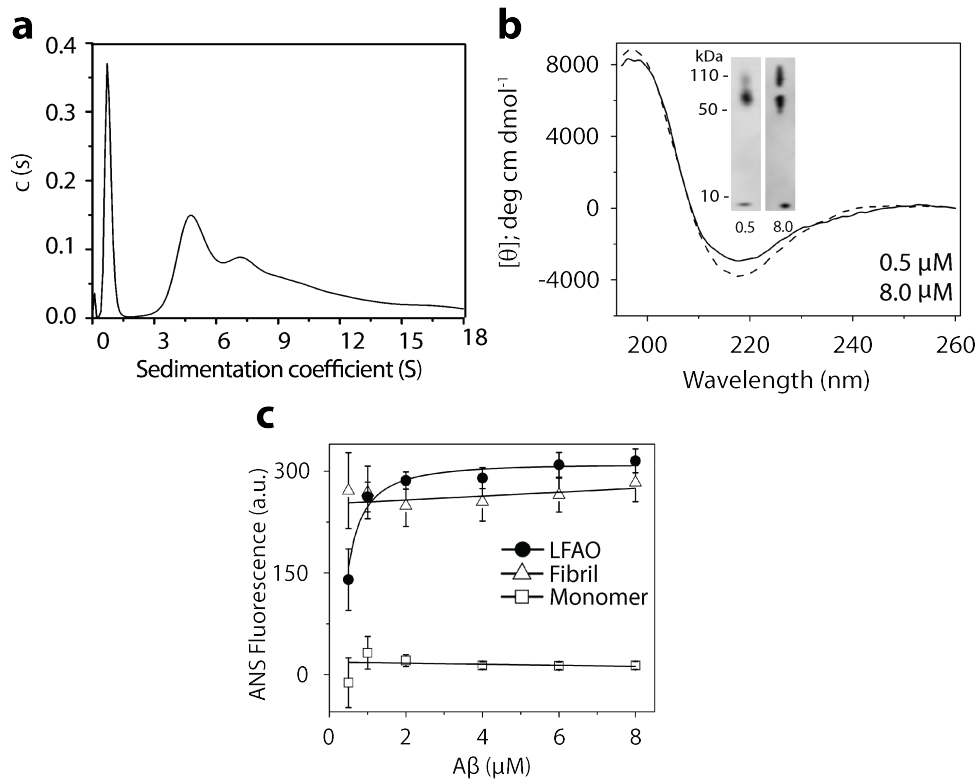


Figure 1. Biophysical characteristics of LFAOs (reproduced from the cited references). (a) LFAOs, as analyzed previously by analytical ultracentrifugation (5) and atomic force microscopy (*inset*, (3)). The single and double arrows represent LFAO 12mer and 24mer, respectively. (b) LFAO (●) concentration-dependent dynamics, as shown previously (2) using ANS fluorescence. A β monomers (□) and fibrils (△) are shown as controls. (c) Circular dichroism spectra and immunoblotting analysis (*inset*) of LFAOs at 0.5 (dashed) and 8 (solid) μ M, as previously described (2).

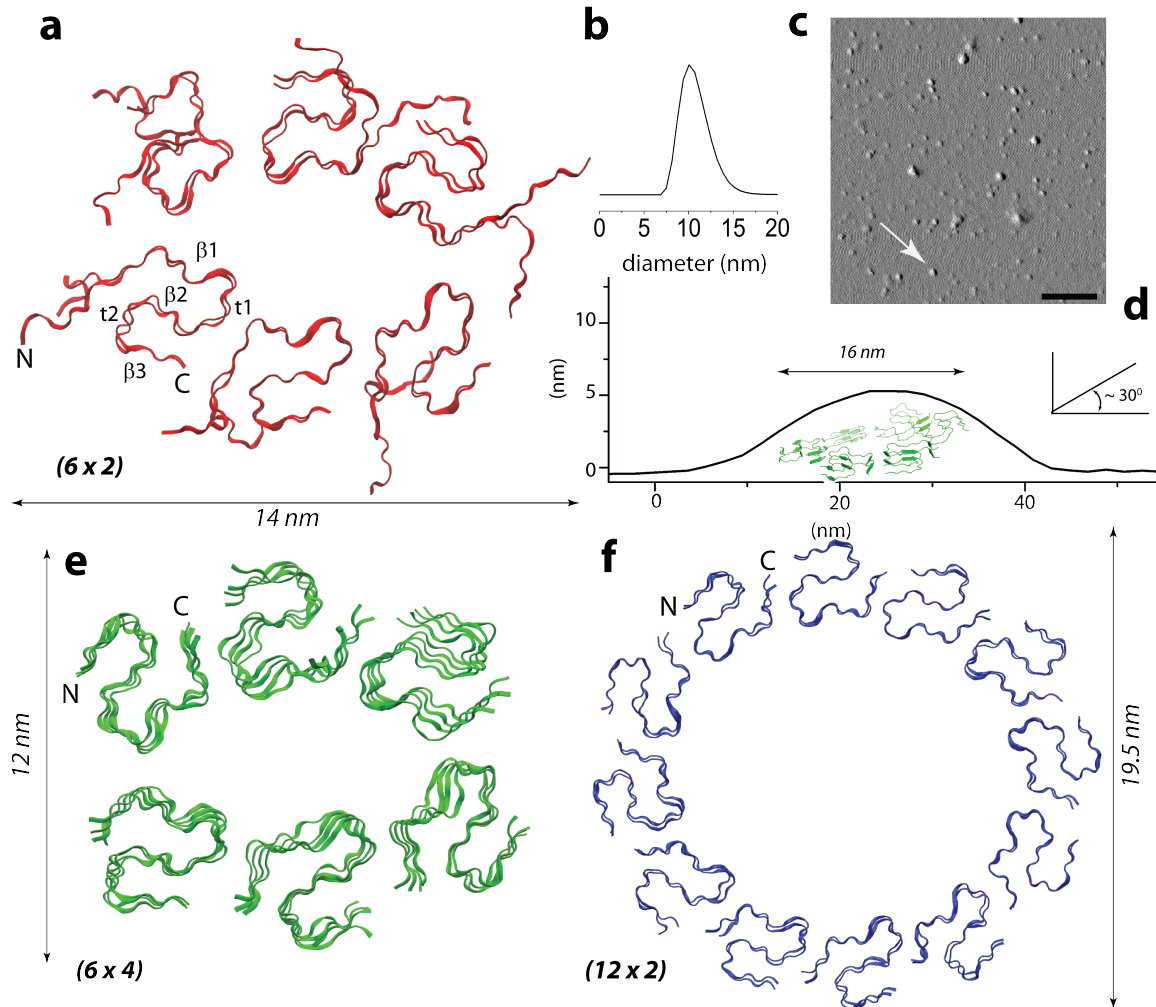


Figure 2. Structural organization of LFAO assemblies. a) The backbone ribbon representation of our (6 x 2) model for LFAO 12mers built from two hexameric rings stacked on top of one another. β-sheets and turns are indicated as β and t. b) DLS measurement shows a monodisperse species with diameter centered at 10 nm. c) AFM image shows punctuate spheres (reproduced from (3)); d) height analysis of one such spherical dot (arrow) in which a (6 x 2) structure is overlaid to show that the height of 5 nm can be accounted for only when the oligomer is at a ~ 30° angle as shown. The corrected diameter of the species is also shown after accounting for cantilever width and scan speed. e and f) possible (6 x 4) and (12 x 2) models for LFAO 24mers along with their diameters.

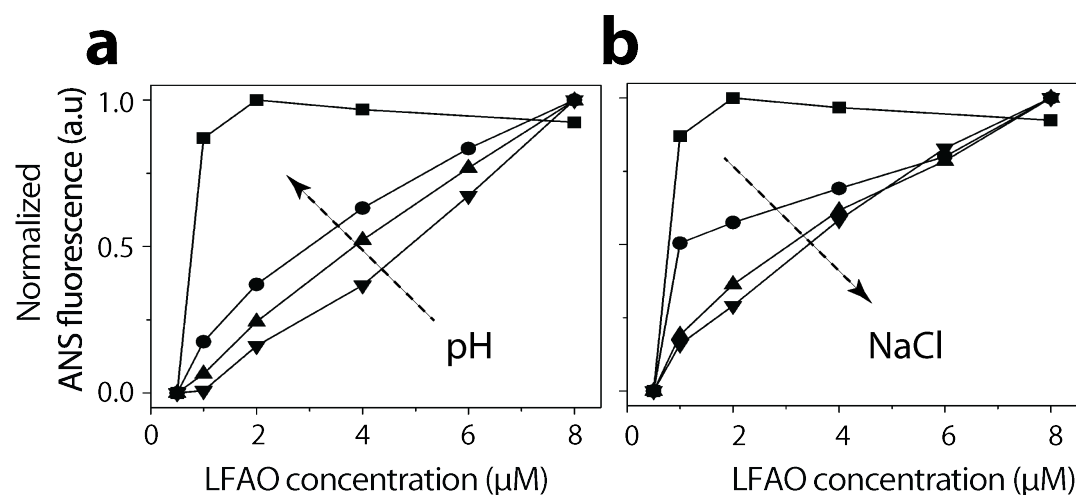


Figure 3. LFAO conformational dynamics at varying NaCl and pH. Normalized ANS fluorescence for 0.5, 1, 2, 4, 6, and 8 μM LFAOs at varying (a) NaCl (0, \blacksquare ; 50, \bullet ; 100, \blacktriangle ; or 200 mM, \blacktriangledown) and (b) pH (8, \blacksquare ; 7, \bullet ; 6, \blacktriangle ; or 5, \blacktriangledown) respectively. Data were processed as described in the Experimental section.

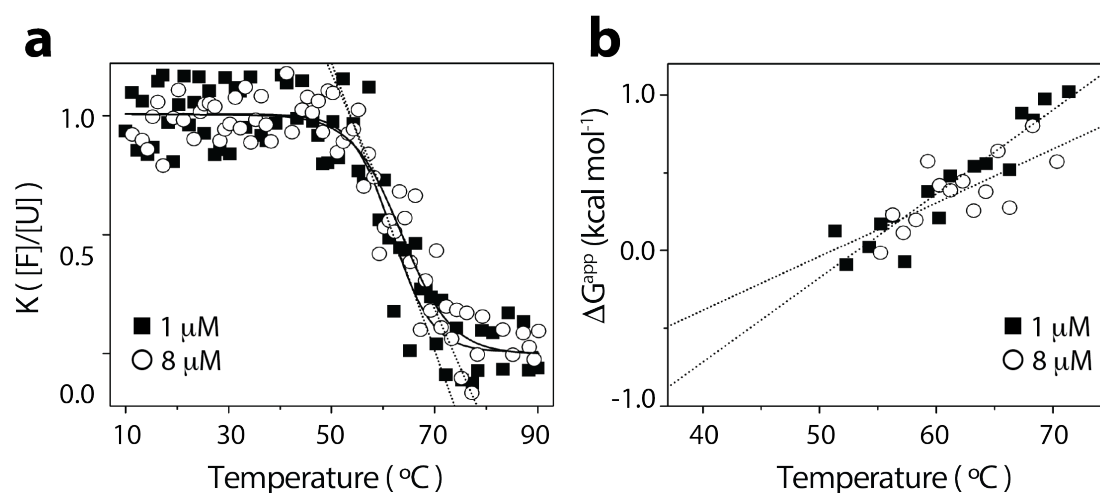


Figure 4. Thermal stability analysis of LFAO 12mer and 12-24mers. (a) Normalized circular dichroism spectra, collected at 206 nm, of 1 (\blacksquare) and 8 (\circ) μM LFAOs upon the addition of SDS (1%) followed by heating to 90 $^{\circ}\text{C}$. (b) The equilibrium constant (K , [folded]/[unfolded]) from panel (a) was used to determine the apparent standard free energy change (ΔG_{app}) for both 1 (\blacksquare)

and 8 (O) μM LFAOs, which was extrapolated to be -0.879 and -0.489 kcal/mol at 37 °C (y-intercept), respectively. The data were process as described in the Experimental section.

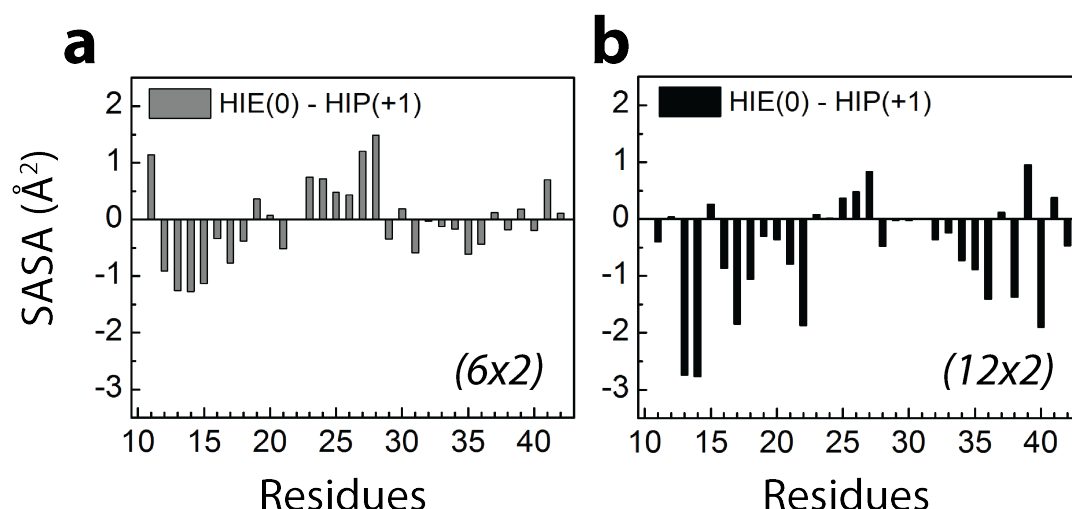


Figure 5. Difference in the solvent accessible surface area (SASA) contributions of single residues between acidic conditions (HIP) and neutral conditions (HIE) for the two A β 42 oligomer models: (a) the (6 x 2) 12mer and (b) the (12 x 2) 24mer.

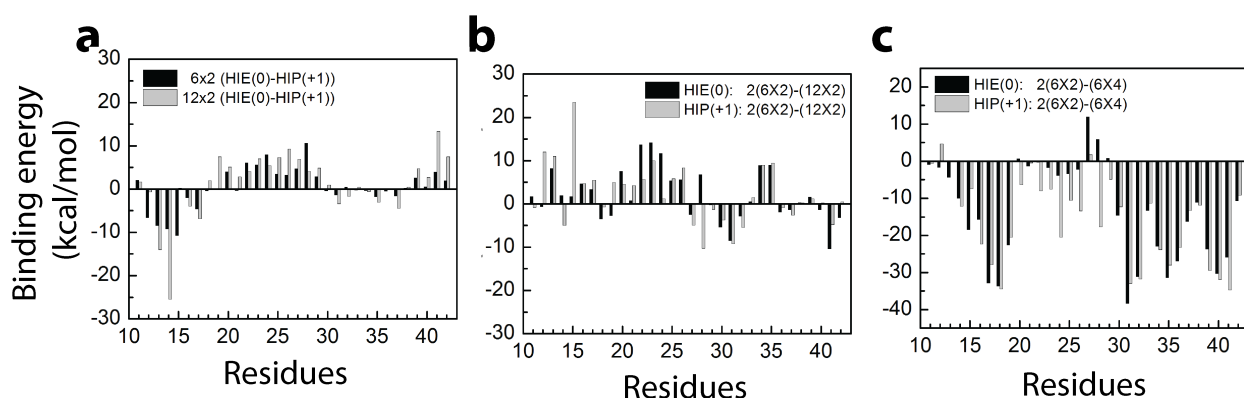


Figure 6. Differences in the binding energy contributions of each residue in the various models. (a) Difference between the values measured under acidic conditions (HIP) and neutral conditions (HIE) for both (6 x 2) 12mer and (12 x 2) 24mer; (b) difference between two times the value measured for the (6 x 2) 12mer and the value measured for the (12 x 2) 24mer, data are

for both acidic conditions (HIP) and neutral conditions (HIE); (c) difference between two times the value measured for the (6 x 2) 12mer and the value measured for the alternative (6 x 4) model for a 24mer, data are for both acidic conditions (HIP) and neutral conditions (HIE);

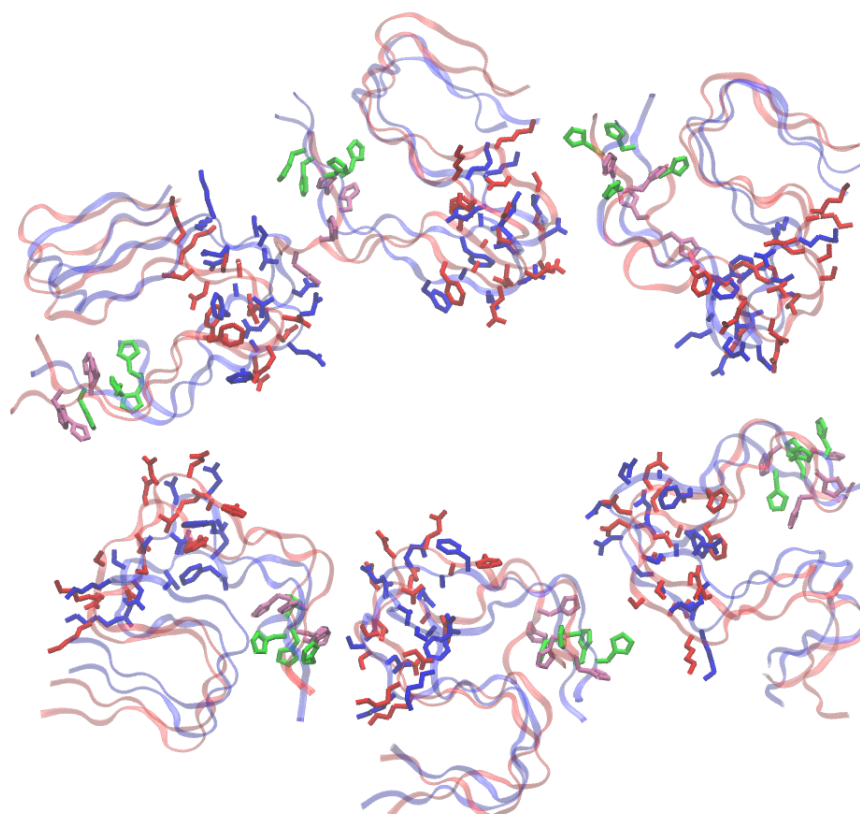


Figure 7. Final structures of the (6 x 2) model for neutral pH (HIE, blue) and acidic conditions (HIP, red) states after a 20ns molecular dynamics trajectory. The sidechains of residues 20 to 28, where the contributions to binding energy differed mostly with pH, are shown in bond representation. The histidine residues H13/H14 are colored in green (HIE) and mauve (HIP).

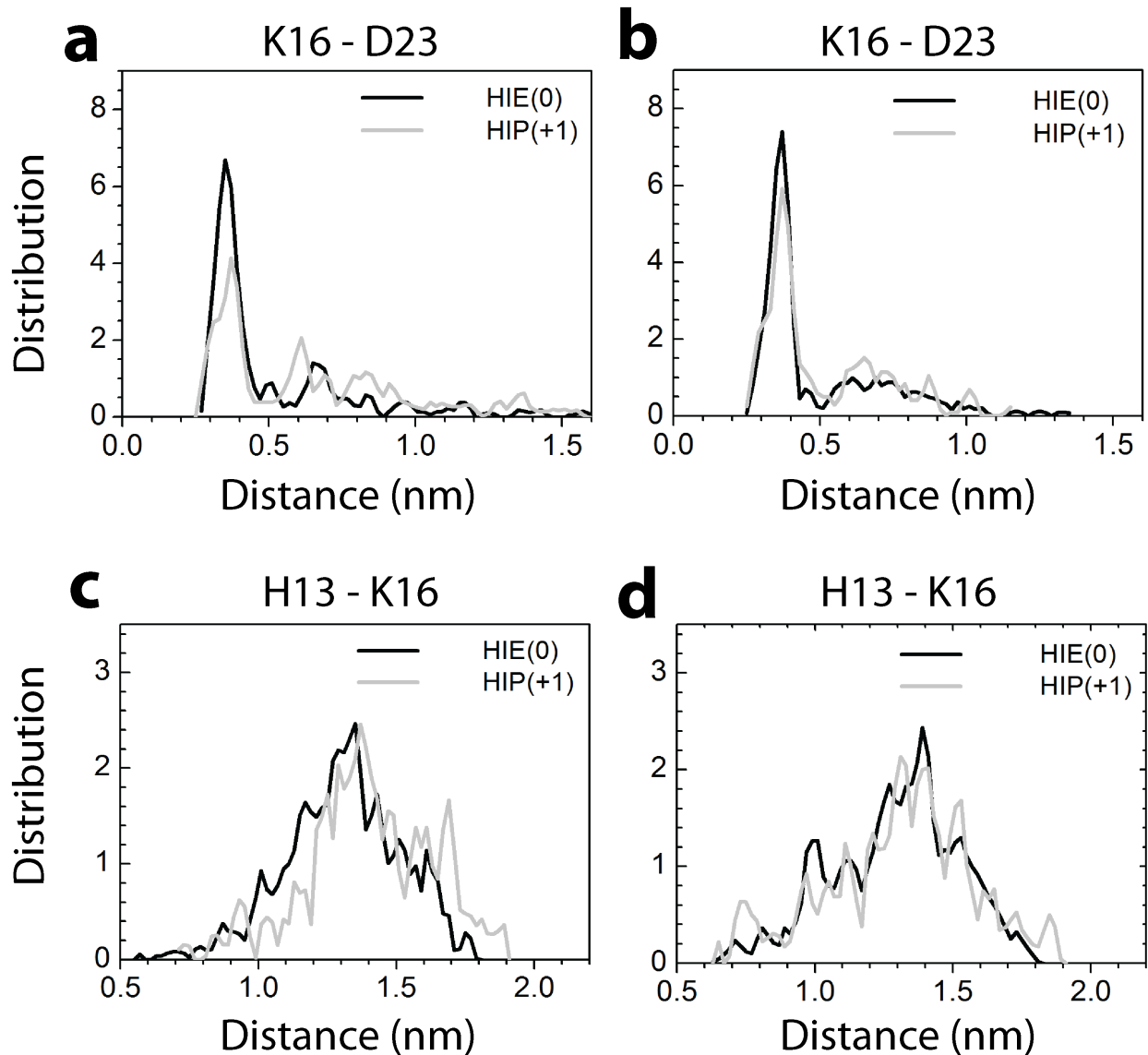


Figure 8. Distance distribution plot. The distribution of distances between the inter chain salt-bridge forming residue 16 (a positively charged lysine) K16 and residue 23 (a negatively charged aspartic acid) D23 in the (6 x2) 12mer (a) and the (12 x2) 24mer. The corresponding distribution of distances between residue 13 (histidine) H13 and residue 16 (a positively charged lysine) are shown in (c) for the 12mer and in (d) for the 24mer.

Binding energy / kcal/mol		(6 x 2)		(6 x 4)		(12 x 2)	
		Avg.	StD	Avg.	StD	Avg.	StD
	E _{VDW}	-690.4	2.2	-953.1	0.2	-1445.9	1.0
	E _{elect}	-213.3	4.0	478.0	46.8	-429.3	57.3
	E _{GB}	371.9	1.5	-259.3	51.6	757.5	52.7
	E _{surf}	-89.5	0.1	-113.6	0.5	-186.8	1.3
	Total	-621.3	0.4	-848.0	4.4	-1304.5	6.9
SASA / Å ²	g_sasa	250.4	1.3	339.1	0.3	495.2	3.0
	POPS: All	258.4	1.3	400.7	0.6	524.0	3.2
	Hydrophobic	163.9	0.4	255.2	0.4	332.2	2.8
	Hydrophilic	94.5	0.4	145.4	0.2	191.8	0.3
	Delta of binding energy kcal/mol			Avg		StD	
	Δ(A)			-58.04		3.9	
	Δ(B)			392.80		1.8	

TABLE 1. The solvent accessible surface area (SASA) and the binding energy of the three considered oligomer models under neutral pH conditions. Shown are for all quantities the averages (Avg) as obtained from two runs of 20 ns and their standard deviations (StD). The binding energy was calculated in a MMGBSA approximation and is composed by four terms: the van der Waals energy E_{vdw}, the electrostatic energy E_{elect}, a generalized Born approximation of the solvation energy E_{GB}, and solvent surface tension interaction term E_{surf}. The SASA values are calculated by two different tools: g_sasa and POPS. In POPS, the SASA values can be further separated into hydrophobic and hydrophilic contributions. The binding energy are defined as follows: Δ(A)=E_(12x2)-2×E_(6x2), Δ(B)=E_(6x4)-2×E_(6x2)).

Binding energy / kcal/mol		(6 x 2)		(6 x 4)		(12 x 2)	
		Avg.	STD	Avg.	STD	Avg.	STD
	E _{VDW}	-696.1	5.2	-903.6	6.3	-1493.4	20.7
	E _{elect}	-15.4	81.7	972.9	95.8	130.3	65.2
	E _{GB}	167.1	73.0	-760.9	87.0	212.6	48.8
	E _{surf}	-91.0	0.1	-108.3	0.5	-197.6	1.7
	Total	-635.3	3.4	-800	15.6	-1348.0	6.1
SASA / Å ²	g_sasa	249.4	1.6	331.9	1.1	511.3	2.3
	POPS: All	257.6	1.8	389.2	0.9	542.4	2.9
	Hydrophobic	163.6	0.6	249.5	0.6	346.9	2.2
	Hydrophilic	94.0	0.5	139.7	0.4	195.5	0.7
	Difference in binding energy kcal/mol			Average		STD	
	Δ(A)			-71.0		6.4	
	Δ(B)			466.2		4.4	

Table 2. The solvent accessible surface area (SASA) and the binding energy of the three considered oligomer models under neutral pH conditions. Shown are for all quantities the averages (Avg) as obtained from two runs of 20 ns and their standard deviations (StD). The binding energy was calculated in a MMGBSA approximation and is composed by four terms: the van der Waals energy E_{vdW}, the electrostatic energy E_{elect}, a generalized Born approximation of the solvation energy E_{GB}, and solvent surface tension interaction term E_{surf}. The SASA values are calculated by two different tools: g_sasa and POPS. In POPS, the SASA values can be further separated into hydrophobic and hydrophilic contributions. The binding energy are as follows: Δ(A)=E_(12×2)-2×E_(6×2), Δ(B)=E_(6×4)-2×E_(6×2)).